GEOPHYSICS, VOL. 71, NO. 5 (SEPTEMBER-OCTOBER 2006); P. D171–D182, 12 FIGS., 1 TABLE.
10.1190/1.2335419

Characterization of layered anisotropic media from prestack PS-wave-reflection data

Jason E. Gumble[1] and James E. Gaiser[2]

ABSTRACT

Anisotropy and fracture characterization in individual layers is realized through iterative layer stripping corrections of four, converted-wave (PS-wave) synthetic reflection seismic data sets, generated from azimuthally anisotropic (HTI and TTI) models, and a four component (4-C) data set from the Teal South, Gulf of Mexico. The corrections were applied on a layer-by-layer basis to evaluate the efficacy of constant polarization rotation and time-shift operators. Equivalent isotropic models were compared to anisotropic models after layer-stripping corrections using rms amplitude and shear-wave-splitting time-difference maps to quantify and identify inherent errors in estimating seismic polarization parameters. For HTI media radial and transverse components of PS data that have had layer-stripping corrections applied, exhibit incorrect symmetry and orientations. This may adversely affect inversion and/or amplitude-variation with angle offset (AVO) and amplitude versus azimuth (AVA) analysis. Layer-stripping corrections applied to fast and slow (PS1 and PS2, respectively) components exhibit the correct symmetry and orientation. Time differences between PS1 and PS2 are computed using crosscorrelation. Previous studies have addressed some of the problems associated with layer-stripping corrections for the case of vertical fractures (HTI media) and poststack layer-stripping analyses. This study includes an equivalent model with dipping fractures (TTI media) and extends the scope to encompass the effects of anisotropy on prestack data. The results from an application of the same technique are also applied to a limited set of 4-C data from the Teal South project in the Gulf of Mexico. Results are consistent with those of previous studies involving solely poststack 4-C rotation analysis in terms of average, or zero offset, time differences and symmetry orientation. Offset and azimuth amplitude/traveltime variations, however, indicate that there is more information contained in prestack seismic data than 4-C rotation can comprehend.

INTRODUCTION

Anisotropy analysis is important for many reasons, but is particularly important in imaging, because anisotropy will cause distortions in ray geometry (Crampin, 1981; Lynn and Thomsen, 1990). Anisotropy is also an important attribute for characterization of fractured reservoirs, where fractures are often fluid-migration pathways (Tatham and McCormack, 1991). P-wave, S-wave, and the ratio of P-wave to S-wave (V_p/V_s) anisotropy can also be the key to unraveling pore aspect ratio and other lithologic parameters (Crampin, 1978; Hudson, 1981; Thomsen, 1995; Tatham and McCormack, 1991a, provide an excellent review of earlier work). In azimuthally anisotropic media, examination of the effect of constant time shifts and rotations on the amplitudes of prestack converted-wave (PS-wave) seismic data is critical in putting constraints on the rock properties determined through inversion of these amplitudes.

Layer stripping of S-wave birefringence is necessary to isolate the zone of interest, because shallower anisotropic layers can leave an imprint on the anisotropic signal from deeper layers. Layer-stripping techniques include the iterative application of a 2C $\times$ 2C rotation (Alford, 1986) for determining principal axes of symmetry and time-difference corrections (Winterstein and Meadows, 1991a), beginning with a shallow layer and progressively working downward. Although the Alford technique has been successfully applied in a wide range of situations, it is chiefly designed for a controlled polarization source, zero-offset data, such as a vertical seismic profiling (VSP), in the presence of depth-invariant azimuthal anisotropy (Winterstein

Manuscript received by the Editor September 20, 2005; revised manuscript received January 19, 2006; published online September 11, 2006.
[1]University of Texas at Austin, Department of Geological Sciences, John A. and Katherine G. Jackson School of Geosciences, 1 University Station, C1100, Austin, Texas, 78712. E-mail: jgumble@speer.geo.utexas.edu.
[2]WesternGeco, 1625 Broadway, Suite 1300, Denver, Colorado 80202. E-mail: jgaiser@denver.westerngeco.slb.com.

and Meadows, 1991b), and therefore, not well suited to 3D problems. The Alford technique also assumes that the polarization of the split S-waves remain orthogonal to each other — an assumption that remains valid at near offset under ideal circumstances.

A method using propagator matrices (Winterstein and Meadows, 1991a, b), adapted from Lefeuvre et al., (1989), avoids the assumption of orthogonal polarizations and only requires that they are linearly independent. This method also does not rely on information from the shallower layers and therefore avoids the potential for propagation of error (Lefeuvre et al., 1991). However, this method is still limited to zero-offset, or at least near-zero-offset data.

Gaiser expanded the 2C × 2C rotation analysis and layer-stripping technique to PS-wave data (Gaiser, 1997, 1999) by relying on orthogonal source and receiver pairs to construct the 2C × 2C matrix in the absence of a controlled-polarization source. Thomsen (2001) suggested a similar approach. The convolutional model has been used also to generalize the aforementioned applications to surface data techniques (Thomsen et al., 1999). However, in principle, these techniques remain 1D poststack methods that average offset and azimuthal variations of S-wave splitting, and are only zero-offset approximations to full prestack layer stripping. The effects of these techniques on multiazimuthal, multioffset prestack seismic data have never been addressed fully. A true understanding of the information in such data must be obtained before a viable prestack layer-stripping approach can be suggested.

Our objective in this study was to evaluate current poststack layer-stripping procedures involving Alford rotation analysis when applied to prestack PS-wave data. S-wave splitting varies as a function of offset and azimuth, and these variations get averaged during stacking. Although Alford's 1D theory is adequate for poststack data, we anticipate that constant rotations and time shifts are inadequate for prestack data.

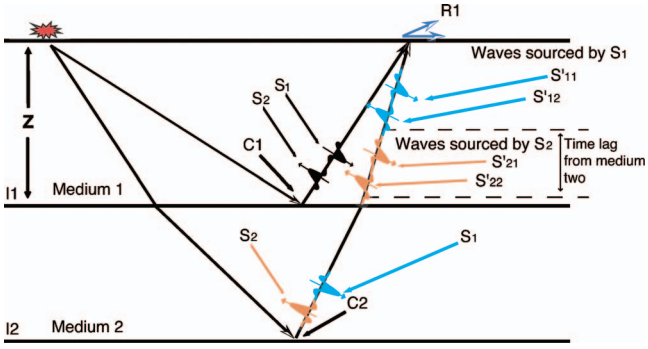

Figure 1. Medium one and medium two are anisotropic. PS-waves are indicated by the respective arrows. R1 indicates the receiver location, and C1 represents the conversion point for waves traveling in medium one only. The polarization and birefringence of these waves may be measured directly at receiver R1. C2 represents the conversion point of waves that will travel through both media. The waves polarize and separate into S_1 and S_2 in the lower medium, and upon incidence with the upper medium at interface I1, each wave will polarize and split again into two new pairs of waves S'_{11}, S'_{12}, S'_{21}, and S'_{22}. This demonstrates how the anisotropy of medium one will be superimposed on that of medium two, causing further birefringence and S-wave rotation.

We approached this study by computing prestack synthetics for transversely isotropic media with a horizontal axis (HTI) and a tilted axis (TTI) to (1) demonstrate the variations with offset and azimuth (important information that is being averaged) and (2) to examine errors of constant orientation and time-shift layer-stripping by comparing isotropic data with layer-stripped anisotropic data. The main contribution of this work is to demonstrate the inadequacies of applying the 1D Alford rotation and layer-stripping method to prestack data, not only for HTI media but also for TTI media in both synthetic data and a field data set from the Gulf of Mexico.

BACKGROUND

The basis for our modeling in this study is that azimuthal anisotropy arises from preferentially aligned cracks or fractures. As is generally asserted, HTI is commonly the result of vertical fractures within a sedimentary layer. Therefore, characterization of the anisotropy of an HTI medium is related to the characterization of the fracture intensity and orientation of the sedimentary layer (Crampin, 1985; Thomsen, 1988). Effective media theory is used to describe a single set, or multiple sets of fractures, in practice today (Helbig, 1958; Schoenberg and Douma, 1988; Bakulin et al., 2000) and generally assuming preferentially aligned, near-vertical, circular, flat cracks. Effective media theory assumes that the fractures occur at a scale less than that of the seismic wavelength. TTI symmetry is the model used here for dipping fractures in horizontally layered media and is simply an HTI medium whose axis is tilted at some angle within a vertical plane.

Layer stripping using PS-waves can be advantageous when performing anisotropic analysis in areas where the seismic signal passes through multiple layers with varying degrees and orientations of anisotropy. The advantage over employing a direct shear-wave (S-wave) source is that the anisotropic signal does not become mixed from layer to layer in both the down-going and up-going legs of the travel path, which have different properties. In contrast, PS-waves are created upon conversion, and only have one up-going S-wave travel path.

S-wave anisotropy may be caused also by horizontal stresses, particularly in the near surface, which may not be related to through-going fractures. It is still critical to characterize this anisotropy fully, regardless of the cause, to make some correction for imaging, as well as isolating the anisotropy in the reservoir and relating this anisotropy to the presence of fractures. It is assumed often that evidence of actual fractures in the target layer is predetermined through other exploratory means such as sonic logs from well borings, direct analysis of oriented core, formation microimager (FMI) logs, etc., and is consistent with that of the current geologic model. In these cases, the anisotropy is assumed to be related to fracturing.

The layer-stripping process attempts to unravel the compounding effects of azimuthal anisotropy on S-waves. Figure 1 shows a layered medium consisting of two anisotropic layers, each with different orientations of symmetry axes for a single-shot and two-component detector. In this example, medium one is anisotropic, and the axes of anisotropy (polarization directions of fast and slow shear waves) are indicated by arrows. The first set of rays in medium one indicates the propagation direction of a compressional wave that converts to shear at point C1.

Medium two is also anisotropic, and a second set of rays indicate the propagation direction of a compressional wave that converts to shear at point C2. A portion of the ray path corresponding to conver-

sion point C2 passes through anisotropic medium one, whose anisotropy will superimpose its polarization on the shear waves, causing further birefringence. The rotation and time shift associated with the split shear wave determined for medium one based on conversion point C1 are applied to all components of data encapsulating medium two, based on conversion point two. Ideally, this procedure will nullify the anisotropic effects of all the layers above the target. The rotation process can be repeated then for many additional layers (after Gaiser, 1997).

The synthetic data computed in this study are based on the Cymric oil field in California, the subject of previous studies using VSPs (Winterstein and Meadows, 1991b), where it was shown that layer-stripping methods can be used to analyze shear-wave birefringence as it changed with depth. Layer stripping has been conducted using poststack seismic analytical techniques (Gaiser and Van Dok, 2003) where the relevance of fracture characterization was demonstrated in the Emilio field in the Adriatic Sea (Gaiser et al., 2001) but was limited to constant time shifts and polarization rotations.

In this study, this analysis has been extended to a subset of the Teal South survey from the Gulf of Mexico. In the Teal South area, at least at the interval under analysis, the sediments were unconsolidated and unlikely to support open fractures. Lynn reported the detection of azimuthal anisotropy in similarly soft sediments in two sites near the San Francisco Bay area (Lynn, 1991, 1992). Her analysis led to the conclusion that the anisotropy was induced by a combination of factors. Two of the factors discussed by Lynn were possible causes of azimuthal anisotropy in the Teal South survey. They are (1) depositional agent or fabric anisotropy and (2) stress-aligned fluid-filled microcracks or extensive dilatancy anisotropy (EDA) (Lynn, 1991, Crampin, 1977, 1978, 1981, 1985).

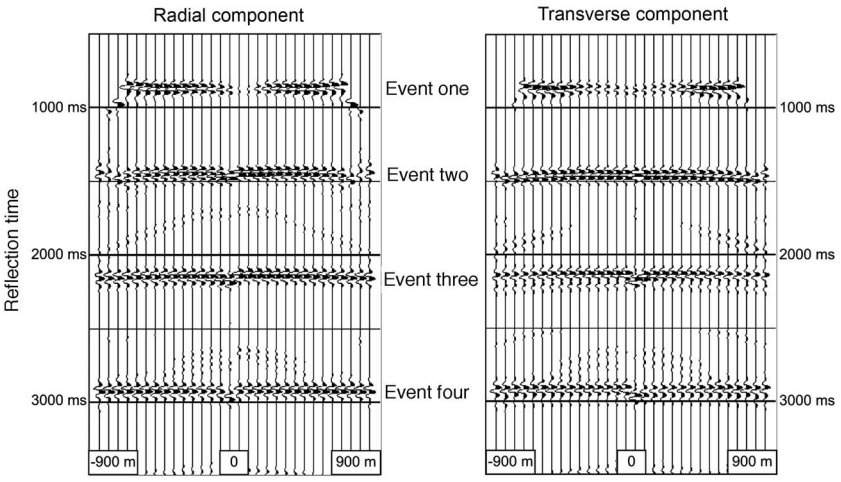

Figure 2. Radial and transverse components from the Cymric HTI modeled seismic data set. Shown here is a 2D line running east-west. The source is located at near-zero offset.

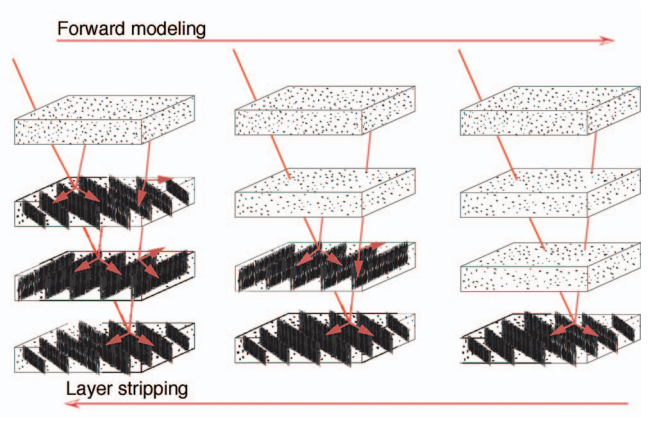

Figure 3. Idealized figures showing a series of models. They illustrate two concepts: (1) one layer of isotropy above three layers of anisotropy as they are consecutively layer-stripped to nullify the birefringent propagation effects of anisotropy and (2) a series of models used for calibration in which the first has three anisotropic layers, the next has two anisotropic layers, etc.

MODELING AND PROCESSING

Four sets of models were produced for the Cymric oil field. The first is a set of models with HTI symmetry (Figure 2) and a corresponding set of isotropic models for comparison. The second set is identical in all respects but is generated with TTI symmetry and its own corresponding set of isotropic reference models. The generation of the reference models makes possible the comparison between the results of the layer stripping for the anisotropic media and those of the equivalent isotropic media (Figure 3). A total of four synthetic models are created for each fracture set (HTI and TTI). In the HTI model, the first layer is isotropic, followed by three anisotropic layers. This model is the subject of the layer stripping and is accompanied by three more models, each with one anisotropic layer replaced by an equivalent isotropic layer, including a four-layer isotropic model (Table 1).

Analysis of the isotropic reference models showed us the ideal case in which there are no anisotropic effects. We can then compare anisotropic models with the corrections applied to the reference models to see how well — or poorly — we have nullified the effects of the anisotropy.

For example, layer stripping corrections were applied for the first anisotropic layer of the HTI model and compared to a model in which the first two layers are isotropic (Table 1). This affords us the opportunity to quantify the error induced by constant rotation and time-shift operators: azimuthal and offset variations in S-wave splitting-time difference, amplitudes and polarizations (a polarization analysis, however, was beyond the scope of this study).

All models are generated using commercially available modeling software, which uses contour integration in the complex frequency-wavenumber domain to compute seismograms and thus produce correct, interpretable amplitudes (Mallick and Frazer, 1987). The models are generated with an impulsive source located in the top isotropic layer to avoid generating direct shear energy. Direct waves, surface waves, and interbed multiples were omitted also. Only one P-wave impedance contrast exists between the top isotropic layer and the second anisotropic layer. For the rest of the model, both P-wave velocity and density remain constant. Only the S-wave

velocities changed from layer to layer to minimize the amount of P-wave energy and isolate the PS-wave. The modeling geometry consists of a single source located in the center of a grid of 30 × 30 receivers, placed at 100 m intervals, and the input wavelet has a frequency of 10-40 Hz.

In order to preserve true amplitudes, minimum processing was applied to the data. Using industry standard processing software, geometry description was defined and a spherical divergence correction applied. The x and y components recorded at the receiver position were rotated to radial and transverse orientations using two component trigonometric rotation. Velocity analysis was performed on the radial component, which included a higher-order moveout correction. The higher-order moveout was determined using a scanning technique which applied the equation:

Table 1. The initial starting models used to compare HTI, TTI, and isotropic media as well as the successive layer-stripped models and their corresponding isotropic reference models. Pre-layer strip: The initial HTI and HTI reference model and TTI and TTI reference models, where θ indicates fracture azimuth in degrees from north, ϕ indicates the antidip, or compliment of the dip angle, of the fractures (where applicable) and γ (v) is the exact Thomsen parameter of the equivalent VTI media. After First layer strip: The same models, indicating that the first anisotropic layer of both the HTI and TTI model have been layer-stripped, i.e., have had constant time shift and rotation applied in an attempt to nullify the anisotropy. Second layer strip: The second anisotropic layer of both the HTI and TTI models have had constant time shift and rotation applied. New reference models are required for comparison, as indicated. Target layer strip: For investigative purposes, the target layer also has had constant time shift and rotation applied. New, purely isotropic models are needed for comparison.

Prelayer strip

	HTI model	Reference model	TTI model	TTI reference model
Layer 1	Isotropic	Isotropic	Isotropic	Isotropic
Layer 2	$\theta = 60°$, $\gamma(v) = .062$	Isotropic	$\theta = 60°$, $\phi = 30°$, $\gamma(v) = .062$	Isotropic
Layer 3	$\theta = 75°$, $\gamma(v) = .041$	$\theta = 75°$, $\gamma(v) = .041$	$\theta = 75°$, $\phi = 20°$, $\gamma(v) = .041$	$\theta = 75°$, $\phi = 20°$, $\gamma(v) = .041$
Layer 4	$\theta = 90°$, $\gamma(v) = .020$	$\theta = 90°$, $\gamma(v) = .020$	$\theta = 90°$, $\phi = 10°$, $\gamma(v) = .020$	$\theta = 90°$, $\phi = 10°$, $\gamma(v) = .020$
Layer 5	Isotropic half-space	Isotropic half-space	Isotropic half-space	Isotropic half-space

After first layer strip

	HTI model	Reference model	TTI model	TTI reference model
Layer 1	Isotropic	Isotropic	Isotropic	Isotropic
Layer 2	Layer stripped	Isotropic	Layer stripped	Isotropic
Layer 3	$\theta = 75°$, $\gamma(v) = .041$	$\theta = 75°$, $\gamma(v) = .041$	$\theta = 75°$, $\phi = 20°$, $\gamma(v) = .041$	$\theta = 75°$, $\phi = 20°$, $\gamma(v) = .041$
Layer 4	$\theta = 90°$, $\gamma(v) = 020$	$\theta = 90°$, $\gamma(v) = 020$	$\theta = 90°$, $\phi = 10°$, $\gamma(v) = .020$	$\theta = 90°$, $\phi = 10°$, $\gamma(v) = .020$
Layer 5	Isotropic half-space	Isotropic half-space	Isotropic half-space	Isotropic half-space

After second layer strip

	HTI model	Reference model	TTI model	TTI reference model
Layer 1	Isotropic	Isotropic	Isotropic	Isotropic
Layer 2	Layer stripped	Isotropic	Layer stripped	Isotropic
Layer 3	Layer stripped	Isotropic	Layer stripped	Isotropic
Layer 4	$\theta = 90°$, $\gamma(v) = 020$	$\theta = 90°$, $\gamma(v) = 020$	$\theta = 90°$, $\phi = 10°$, $\gamma(v) = .020$	$\theta = 90°$, $\phi = 10°$, $\gamma(v) = .020$
Layer 5	Isotropic half-space	Isotropic half-space	Isotropic half-space	Isotropic half-space

After target layer strip

	HTI model	Reference model	TTI model	TTI reference model
Layer 1	Isotropic	Isotropic	Isotropic	Isotropic
Layer 2	Layer stripped	Isotropic	Layer stripped	Isotropic
Layer 3	Layer stripped	Isotropic	Layer stripped	Isotropic
Layer 4	Layer stripped	Isotropic	Layer stripped	Isotropic
Layer 5	Isotropic half-space	Isotropic half-space	Isotropic half-space	Isotropic half-space

$$t_x^2 = t_0^2 + \frac{x^2}{Vp_n^2} - \frac{2\eta x^4}{Vp_n^2[Vp_n^2 t_0^2 + (1+2\eta)x^2]} \quad (1)$$

(Alkahlifah and Tsvankin, 1995) where t_x is the total traveltime to offset x, t_0 is the zero-offset traveltime, and x is the source-receiver offset distance. Vp_n is the short-spread PS-wave velocity and η is the effective parameter used to reduce differences between the Thomsen parameters ϵ and δ. The effective parameter η is then replaced by κ, an equivalent P-SV velocity parameter (Cheret et al., 2000). The equation was applied to normal moveout (NMO) corrected source gathers for several values of κ and the best correction was picked using a visual screening technique.

The next step is to apply this higher-order correction to both the radial and transverse components. A spherical divergence correction, using a TV^2 parameter, where V is the rms PS-wave velocity determined from velocity analysis, is then applied to both components.

Amplitude analysis of radial and transverse components for a wide range of source-receiver azimuths is used to determine the principal axes. Root-mean-square amplitudes are extracted across the events in question from the moveout corrected receiver gathers and are used to graphically interpret the principal directions of the fractures. Once the radial and transverse components are rotated to fast and slow polarizations (PS1 and PS2), respectively, a crosscorrelation is made between the fast and slow waves. From the crosscorrelation results, time-difference maps are constructed and compared with PS-wave rms amplitude maps for analysis. Once a constant (average) shift has been determined, PS2 was shifted and the data rotated back to radial and transverse components. The radial component of the layer-stripped model is then compared to the radial component of the equivalent isotropic model to quantify further the azimuthally dependent errors associated with the constant shift.

LAYER STRIPPING AND CALIBRATION

Cymric model

Amplitudes are extracted from time windows centered about the reflection of the event in question to characterize the principal axes of the layer beneath the reflector. For both HTI and TTI symmetries, the amplitudes from an isotropic layer over an anisotropic layer (referred to as event one in the analysis) provides a baseline for the amplitudes that can be used to estimate the principal directions of the anisotropy (Figure 4). There is no time difference between the fast and slow components, but the amplitudes of the radial and transverse components are indicative of the anisotropic layer beneath the event because the S-waves polarize to the principal directions upon reflection.

In the HTI case (Figure 4a–d), the rms amplitudes of the radial

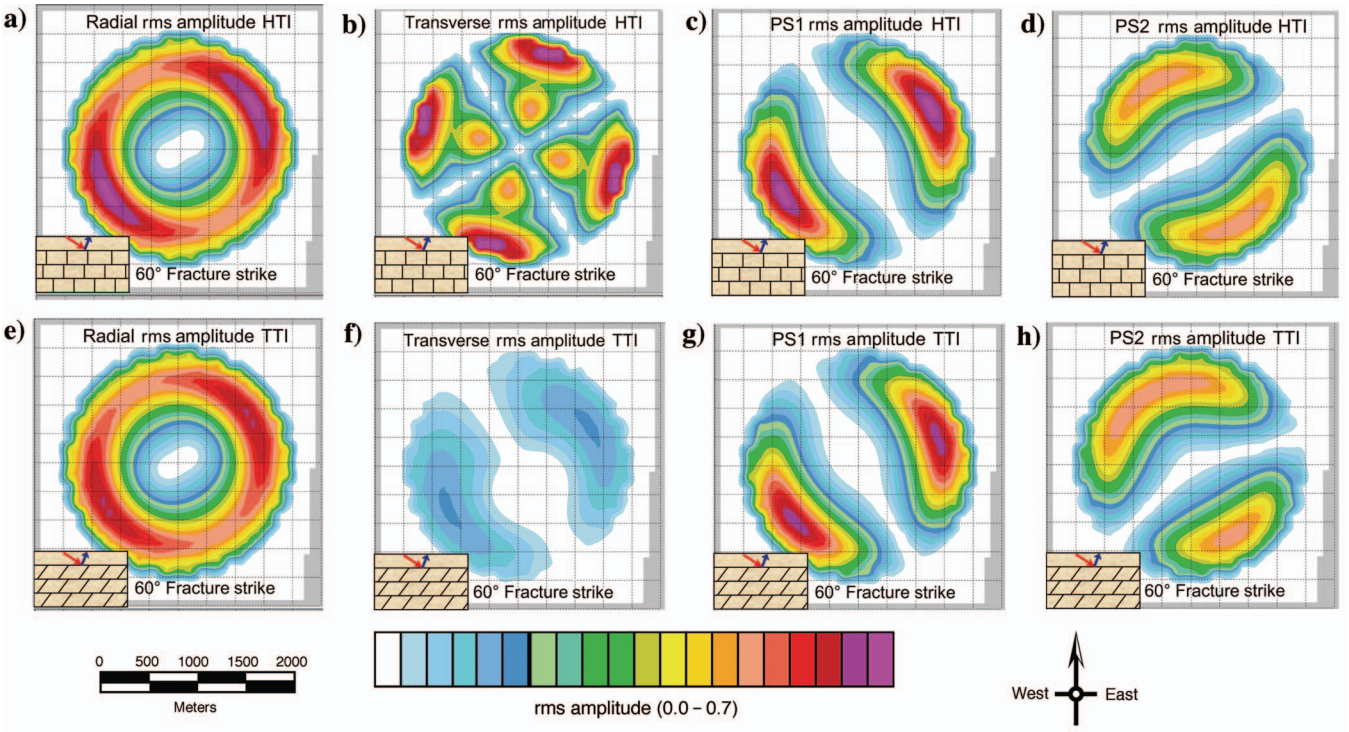

Figure 4. Baseline rms amplitude for reflection event one. Shown are the rms amplitudes extracted over a window corresponding to the reflection pictured in the model icon. For this and all subsequent figures, the rms amplitudes are shown in plan view with the source located in the center and receivers across the entire grid. Within the model icon the red and blue arrows represent the ray path to the event in question; vertical lines within the layer represent HTI media, whereas dipping lines within the layer represent TTI media. In subsequent icons the dotted lines between events represent layers that have been layer-stripped. In the first example the medium is isotropic over anisotropic with HTI results shown on the left (a–d.) with fractures in the medium below, oriented at 60° and TTI results shown on the right (e–h.) with the same fracture set, with an antidip of 30° to the northwest. (a) The rms amplitude of the radial component in HTI media. The signature is a dipole inline with the strike of the fractures which lie beneath. (b) The rms amplitude of the transverse component is a quadrapole with the nulls both inline and perpendicular to the fracture strike. (c) The rms amplitude of the component rotated inline with the fractures. (d) The rms amplitude of the component rotated perpendicular to the fractures. (e) The rms amplitude of the radial component in TTI media. (f) The rms amplitude of the transverse component in TTI media. (g) The rms amplitude of the component rotated parallel to the fracture strike. (h) The rms amplitude of the component rotated perpendicular to the fracture strike.

component from event one (Figure 4a) can be characterized as a dipole, with the two poles, or regions of greater amplitude, pointing toward the principal axes of the anisotropy of the underlying layer. The rms amplitudes of the transverse component (Figure 4b) have a quadra-polar distribution, or quadrapole, approximately zero offset with equal amplitude partitioned to each pole. The polarity of the amplitude in each pole changes about the symmetry axis; however, this is not shown or discussed in this paper, but may be a useful indicator in subsequent investigations. The nulls of the poles are inline with and perpendicular to the axes of symmetry of the layer beneath. PS1 and PS2 rms amplitudes from the same event (Figure 4c and d) show greater amplitude near the underlying fracture strike (on PS1), relative to the amplitude perpendicular to the fracture strike (PS2).

The TTI case differs slightly from the HTI case (Figure 4e–h). The TTI radial component amplitude (Figure 4e) exhibits virtually the same symmetry as in the HTI case yet is diminished somewhat (lower peak amplitude) when compared to the HTI case. The transverse component reflectivity (Figure 4f) is affected dramatically by the dip of the fractures in the lower medium. The expected quadrapole observed in the HTI case is replaced by an amplitude signature that is similar in appearance to that of the PS1 amplitude and is diminished also in amplitude relative to that of the HTI case. A possible reason for this is a relatively low S-wave impedance contrast at this event,resulting in a high sensitivity to the fracture dip, which in this case is quite large (30° antidip). In the case of the fast and slow components (Figure 4g and h), there is an observable variation from the HTI case, corresponding to the direction of the fracture dip (to the northwest). The PS1 component peak amplitudes are shifted slightly up dip whereas the transverse component amplitude shows a greater peak in the down dip of the fracture direction.

The amplitudes extracted from event two, an anisotropic layer over anisotropic layer reflection, are indicative of the second layer'sfracture strike as well (Figure 5). The radial component rms amplitude (Figure 5a) is now a quadrapole, however, with greater

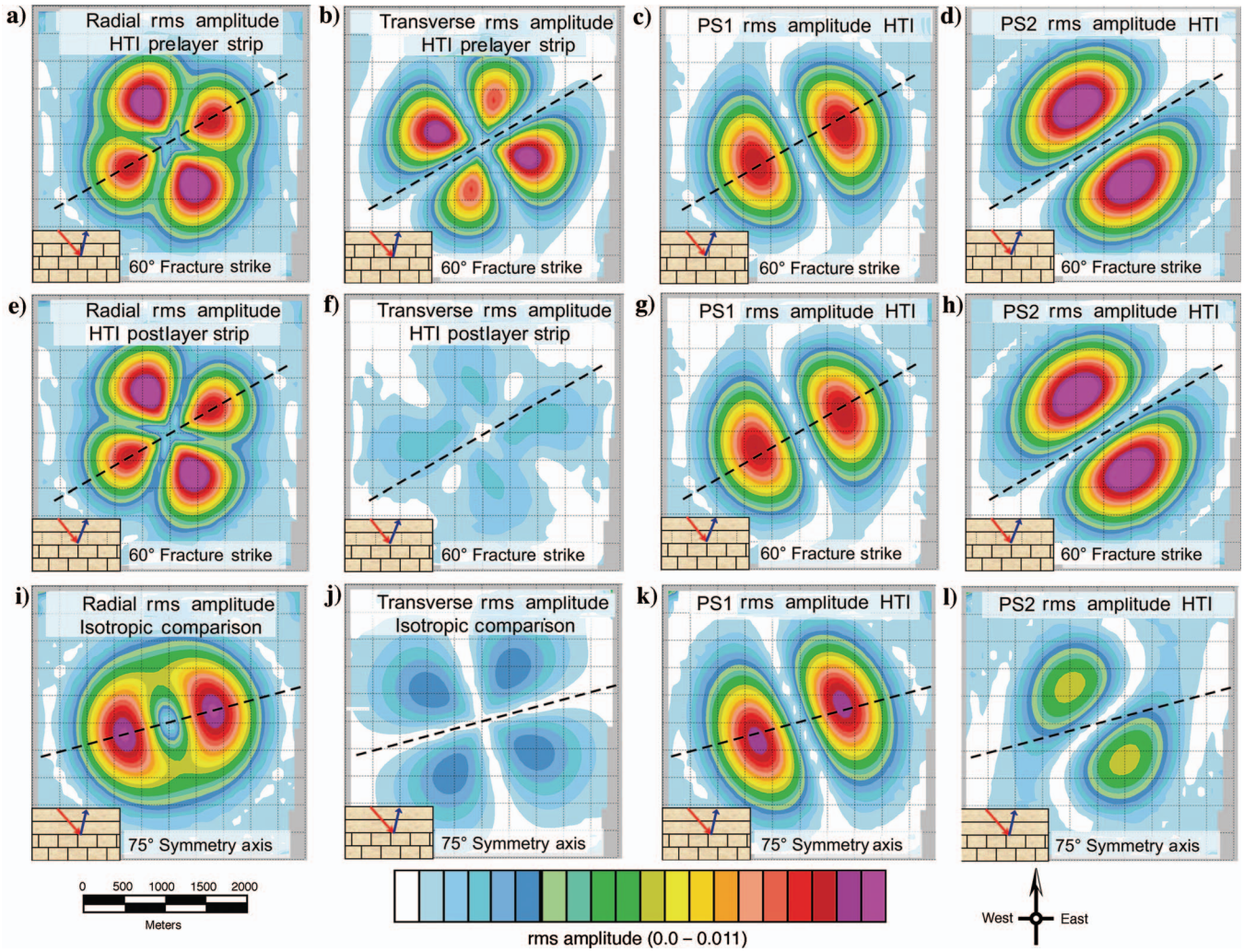

Figure 5. The rms amplitudes for radial, transverse, and fast and slow S-waves from reflection event two, an anisotropic over anisotropic event in a HTI medium. (a, b) Prelayer strip radial and transverse components for HTI. The 60° fracture strike of layer two may be interpreted from the alignment of the dipole. (c, d) The corresponding PS1 and PS2 components for the same event as in (a) and (b). (e, f) Postlayer strip radial and transverse components. (g, h) The corresponding PS1 and PS2 components. Note they are identical to those in (c) and (d) but are included for instruction. (i, j) Equivalent isotropic layer over anisotropic layer radial and transverse component for the HTI medium. In this case they exhibit the fracture strike of layer three beneath (75°). (k, l) The corresponding PS1 and PS2 components. Although PS1 and PS2 are not inline with the HTI symmetry beneath event two (75°), they are rotated to 60° for direct comparison to (a, b) and (g, h).

amplitude on the poles perpendicular to fracture strike of the upper layer. The transverse component amplitude (Figure 5b) is also a quadrapole, the nulls of which are in line and perpendicular with the fracture strike of the upper layer. When rotated to fast and slow orientations (Figure 5c and d), we see greater amplitude in the slow direction, perpendicular to the fracture strike. A bulk time shift is determined from a crosscorrelation made between the fast and slow components in an attempt to reconcile the time difference resulting from the anisotropy of this layer (Figure 6), the analysis of which is detailed hereafter. Layer stripping is then accomplished by bulk shifting the slow component to match the fast. The components are then rotated back into radial-transverse coordinates for comparison.

Amplitudes of the postlayer strip corrected radial component (Figure 5e) are slightly greater in magnitude than those of the prelayer strip radial component (Figure 5a), a result of transferring energy from the transverse component (Figure 5b–f). The transverse energy has been minimized to within a small magnitude expected for the isotropic layer over the anisotropic layer (Figure 5j). When comparing the amplitudes of the radial component that has been layer strip corrected to that of a model that has original isotropy, we see many differences. The radial amplitude of the isotropic over anisotropic model (Figure 5i) is a dipole, whereas the radial amplitude of the layer-stripped model remains a quadrapole. The fast and slow S-waves for the layer-strip corrected case (Figure 5g and h), are virtually identical to that of the prelayer-strip corrected case, but are included for instructional purposes. The fast and slow shear waves of the isotropic over anisotropic reference model (Figure 5k and l) have been rotated to 60° for display, which would not be done in practice, but has been included here for direct comparison to the anisotropic over anisotropic case.

The amplitude of the isotropic slow wave is much lower than that of the layer-strip corrected slow wave, as is expected. The amplitude on the slow component in the isotropic case results solely from the anisotropy of the layer beneath the isotropic event. For clarification, see the model icons located on each panel in Figure 5. Using constant rotation and time-shift operators has caused a distortion in the amplitudes and symmetry axes, relative to the amplitudes and symmetry axes of the equivalent isotropic layer over anisotropic layer model as a result of differences in medium reflectivity.

The amplitudes extracted from event two for the TTI model, differ from the HTI model in that the quadrapoles of the radial and transverse components are slightly off from the principal axes, but still nearly aligned with the second layer's 75° fracture strike (Figure 7a and b). Amplitudes for this event with the layer-stripping correction applied are also distorted (Figure 7e and f). It is difficult to interpret the primary axes; however, the transverse component does approximate the fracture strike. The amplitudes of the fast and slow waves (Figure 7c and d) are comparable to that of the HTI case, although the amplitude difference in line and perpendicular to the fractures is less noticeable, and there is some skew detectable, particularly on the slow component. Again, for completeness, the fast and slow shear waves are shown for the postlayer-strip scenario (Figure 7g and h), although they are equivalent to that of the prelayer strip case. Some insight can be derived from the isotropic counterpart to the model (Figure 7e–l). The radial component has a dipole pattern where higher amplitudes are inline with the 75° fracture strike associated with layer three. The transverse component is indeed a distorted dipole, bent symmetrically about the axis, normal to the fracture strike. When fast and slow waves are rotated to 60°, they show a similar difference in amplitude and resulting skew, as in the HTI case.

After the rotation of radial and transverse components to PS1 and PS2, S-wave splitting-time differences for event two are computed using crosscorrelation. For the HTI medium, the average time shift is determined by choosing the time difference associated with the peak distribution (Figure 6a). For the TTI medium, there are two peaks in the time-difference distribution; consequently, the average time shiftis taken between these two modes. The PS1 and PS2 components, are then rotated back to radial and transverse components, and

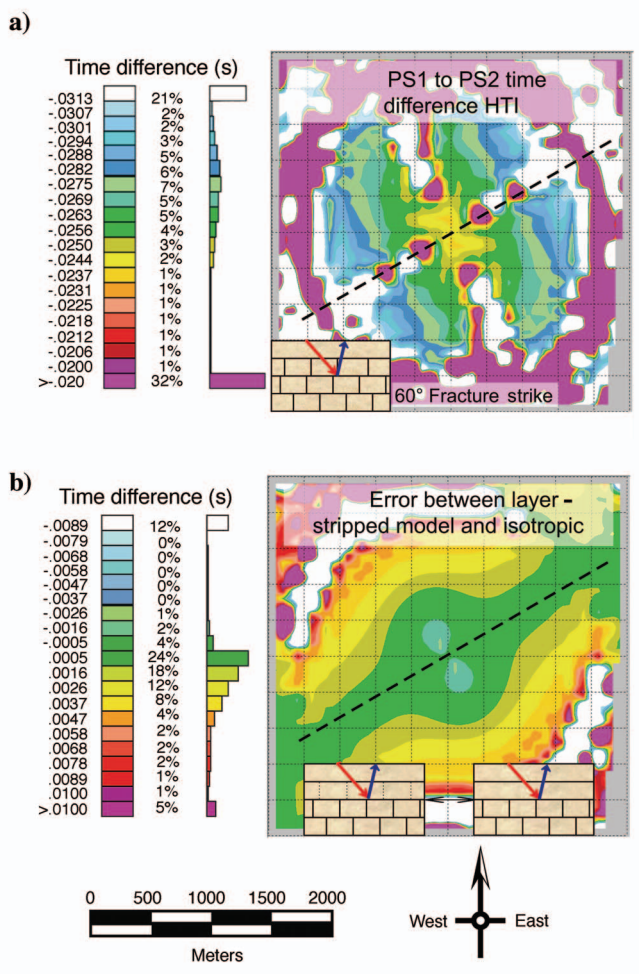

Figure 6. S-wave-splitting time-difference maps for reflection event two resulting from crosscorrelation of the PS1 and PS2 components displayed as constant time-shift color contours. (a) HTI medium: Time differences range from −32 to −24 ms. Offset and azimuthal variations in time differences are a symmetric, elliptical pattern with the long axis perpendicular to fracture strike and the short axis parallel to fracture strike. (b) Time-difference error derived from comparing the layer-stripped model to an equivalent isotropic model. Time differences range from −10 to 10 ms. Offset and azimuthal variations show agreement between the two models at near-zero offset and along fracture strike but disagree at far offsets normal to the fracture strike. The zero time shift lies in the center of the green constant time-shift contour.

the amplitude extraction is performed again. This quantifies the errors associated with a single rotation and timeshift-operator layer-stripping approach.

Another crosscorrelation is performed then to compare the layer-stripped radial component to the radial component from an equivalent isotropic model (Figure 6b). Results from the S-wave splitting analysis resolve subtleties in the time differences between PS1 and PS2 (Figure 6a) beyond those observed in the seismograms. An elliptical pattern of time difference is symmetrical with respect to the principal axes. The lack of data along the principal axes results from low signal where S-wave splitting is minimal. Figure 6b shows there is no transverse data along the principal axes to analyze. Despite this, a clear, elliptical pattern is resolvable for the HTI medium, indicating the extent of azimuthal and offset variations. The short axis of the ellipse is parallel to fracture strike, whereas the long axis is perpendicular to fracture strike. An average time difference can be chosen based on the peak distribution of time differences shown in the legend. In this case, an average shift of ~27 ms was chosen. If we compare the layer-stripping corrected model to the isotropic model, we can map the time difference errors resulting from the bulk shift. Results show a symmetric pattern about the fracture strike where the area of greatest agreement is at near-zero offset and along fracture strike, with increasing error normal to fracture strike as offset increases.

S-wave-splitting time-difference maps of event three for the TTI model no longer exhibit an obvious elliptical pattern, but azimuthal and offset variations show only one plane of symmetry in the dip direction of the fractures (northwest-southeast, see Figure 8a). The av-

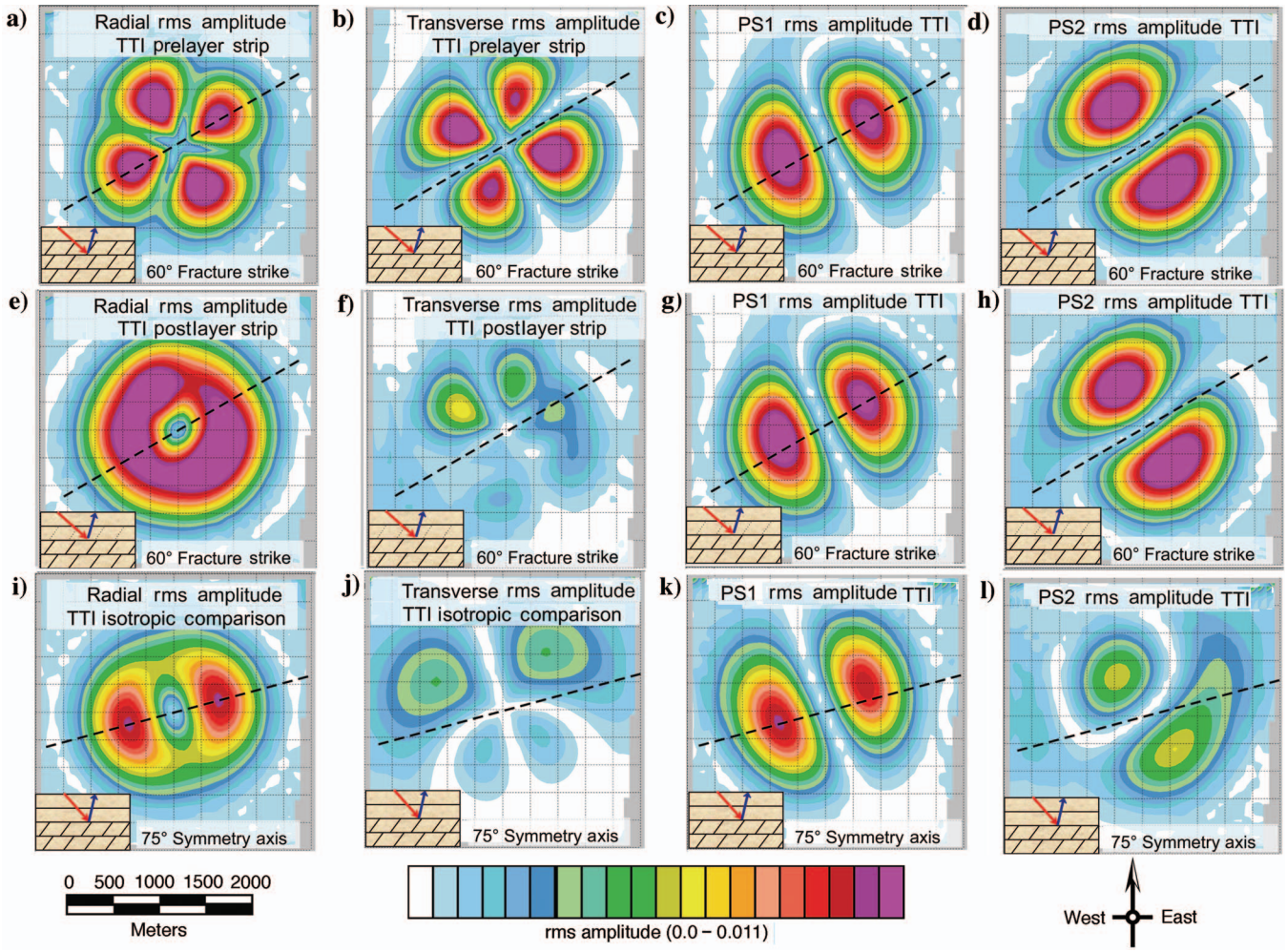

Figure 7. The rms amplitudes for radial, transverse, and fast and slow S-waves from reflection event two, an anisotropic over anisotropic event in TTI medium (a, b) Prelayer strip radial and transverse components for TTI media. The 60° fracture strike of layer two may be interpreted from the amplitudes. (c, d) The corresponding PS1 and PS2 components for the same event. (e, f) Postlayer-strip radial and transverse components. (g, h) The corresponding PS1 and PS2 components. Note they are identical to those in (c) and (d) but are included for instruction. (i, j) Equivalent isotropic layer over anisotropic layer radial and transverse components for the TTI medium. In this case they exhibit the fracture strike of layer three beneath (75°). (k, l) The corresponding PS1 and PS2 components rotated to 60°. Although PS1 and PS2 are not inline with the HTI symmetry beneath event two (75°), they are rotated to 60° for direct comparison to (a, b) and (g, h).

erage timeshift is calculated by taking an average between the two peaks on the time-shift distribution scale. The layer-strip-corrected radial component was compared again to the isotropic radial component for event two. The results now show an asymmetric pattern about the fracture strike (Figure 8b) where the area of greatest agreement is no longer near-zero offset, although there is a trend along fracture strike with increasing error normal to fracture strike as offset increases.

Teal South survey

An identical analysis was made of a single receiver gather from the Teal South data (Figure 9). Although the cause(s) of anisotropy in the soft sediments at Teal South is not the same as in the previous modeling examples, the analytical techniques remain identical. Azimuthal anisotropy has been observed in soft sediments (Lynn, 1991) and as discussed above, similar mechanisms may explain our observations as well.

Radial and transverse component amplitudes of shallow-reflection events were analyzed in the manner discussed above in order to detect azimuthal anisotropy. Events analyzed are described as events 1–4 (Figures 10 and 11) and are progressively deeper. Event one (Figure 10a and b) is characterized as isotropic. The amplitude of the radial component is nearly circular, and there is little energy on the transverse component.

The second event is characterized as isotropic as well (Figure 10c and d), although there is some elongation of the amplitude signature of the radial component and the beginnings of a quadrapole on the transverse component. We compare the amplitudes of event three to that of the modeled case in which we have an isotropic layer over an anisotropic layer (Figure 4) because both the radial and transverse components display similar characteristics. The radial component in the Teal South event three (Figure 10e) may be characterized as a dipole with greater amplitudes aligned at 115°. The amplitude of the transverse component (Figure 10f) has evolved into a recognizable quadrapole. From the S-wave splitting-time-difference map (Figure

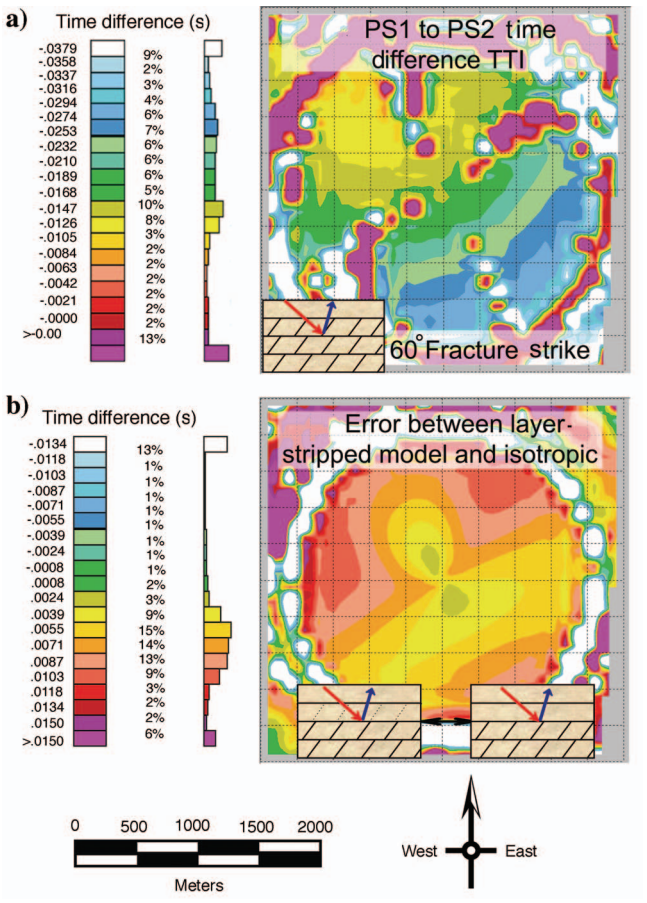

Figure 8. S-wave-birefringence maps for reflection event two resulting from crosscorrelation of the PS1 and PS2 components displayed as constant time-shift color contours for TTI model data. (a) TTI medium: Time differences range from about –32 to –12 ms, but the offset and azimuth variations in time differences are asymmetric where the elliptical pattern is distorted as a result of fractures dipping 60° (in layer two) to the northwest. (b) Time-difference error derived from comparing layer-stripped model to an equivalent isotropic model. The pattern of time-shift errors is asymmetric about the fracture strike. Time differences increase down dip (northwest) and decrease initially updip (southeast). In contrast to the HTI example, the area of lowest error is no longer along fracture strike, but is around zero offset.

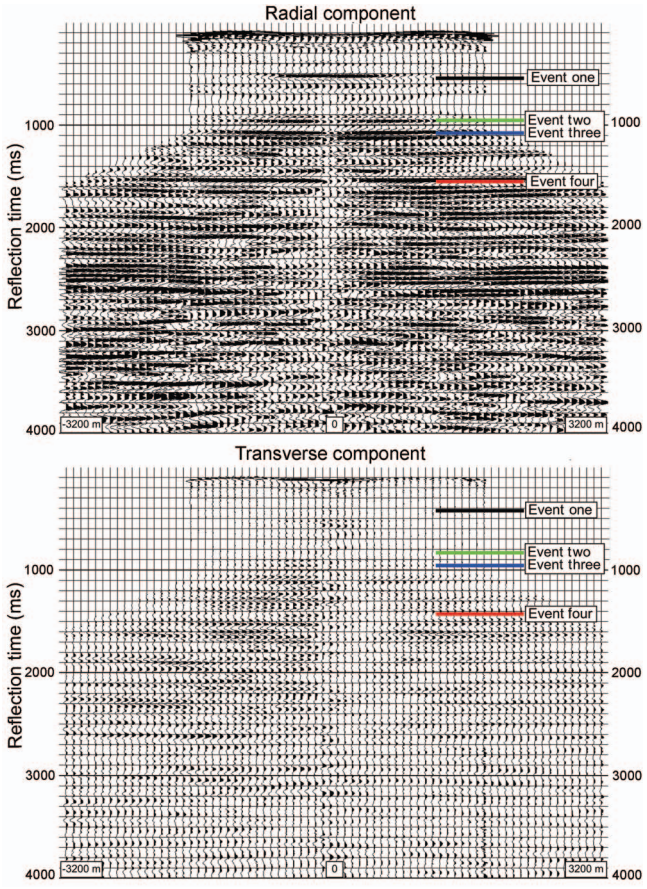

Figure 9. Radial and transverse components from a portion of a receiver gather from the Teal South data set.

12a) it is possible to discern an average time shift of 7.5 ms for eventthree. These time differences display none of the previously observed symmetries of the elliptical or dipping elliptical pattern observed in HTI and TTI models, yet there is some symmetry associated about the principal axes.

An earlier poststack Alford rotation analysis (Alford, 1986) indicated similar symmetry orientations for event three, but found only a 1- or 2-ms average time shift for the upper layer (Stewart et al., 2003). However, the poststack Alford rotation and layer-stripping analysis is sensitive to NMO errors and averages azimuthal traveltime measurements, making it insensitive to the offset and azimuthal traveltime measurements and may not result in the correct answer. Alford analysis may be complicated also by azimuthally variant static variations. Without having the benefit of previous studies, the amplitudes in the previous event may have been interpreted as registering from an isotropic layer overlying an anisotropic layer because the radial component exhibits a dipolar amplitude pattern.

Taking event three as the reflection from the top of an anisotropic layer, an event located at approximately 1550 ms was interpreted to be from an interface between an anisotropic over an anisotropic layer (Figure 11). The amplitude of the radial component (Figure 11a) may be described as a quadrapole, similar to those noted for anisotropic over anisotropic events for the modeled HTI and TTI examples (Figures 5 and 7). The transverse component (Figure 11b) also compares well to the models. As in the models upon layer stripping, the amplitude of the radial component (Figure 11c) has grown slightly, whereas the transverse component (Figure 11d) has been minimized, although the amplitudes of each component remain in a quadrapole. The fast and slow components (Figure 12e and f) have amplitudes indicative of an HTI medium, with little or no skew, indicating the correct symmetry axis has been used for rotation. From the time-difference map (Figure 12b), a time difference of 14 ms was determined and agrees with previous Alford rotation analysis.

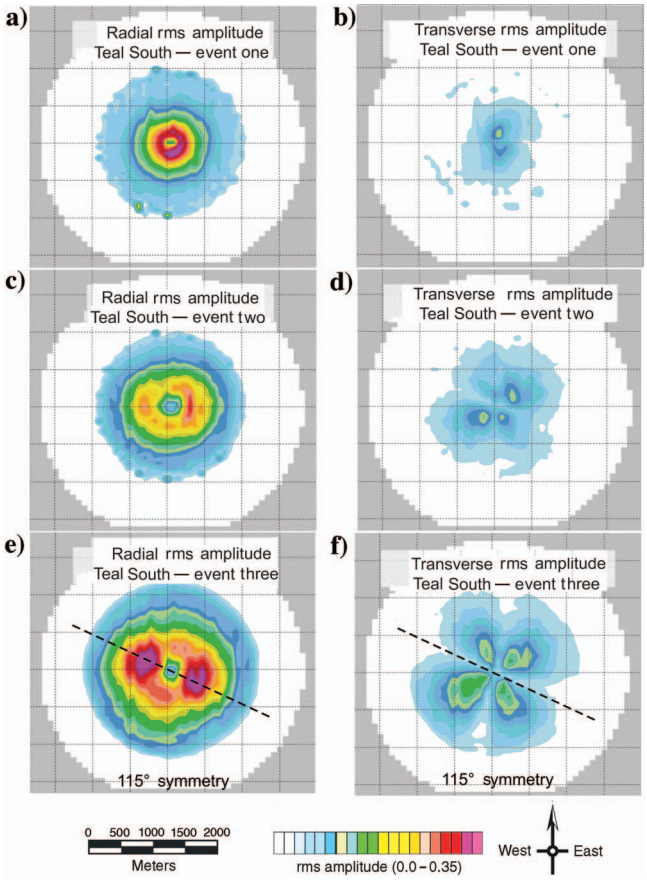

Figure 10. The rms amplitudes for the radial and transverse components for three events from the Teal South data set. (a, b) This event is interpreted as isotropic, having a nearly circular pattern of rms amplitude on the radial and transverse components. (c, d) Radial and transverse components for event two, lower in the section. This event also is characterized as isotropic, although there is some elongation in an east-west direction on the radial component and the beginnings of a quadrapole on the transverse component. (e, f) Radial and transverse components from event three. The event is characterized as an isotropic layer over an anisotropic layer. The radial component is a dipole aligned at approximately 115°. The transverse component is a quadrapole aligned at 115°.

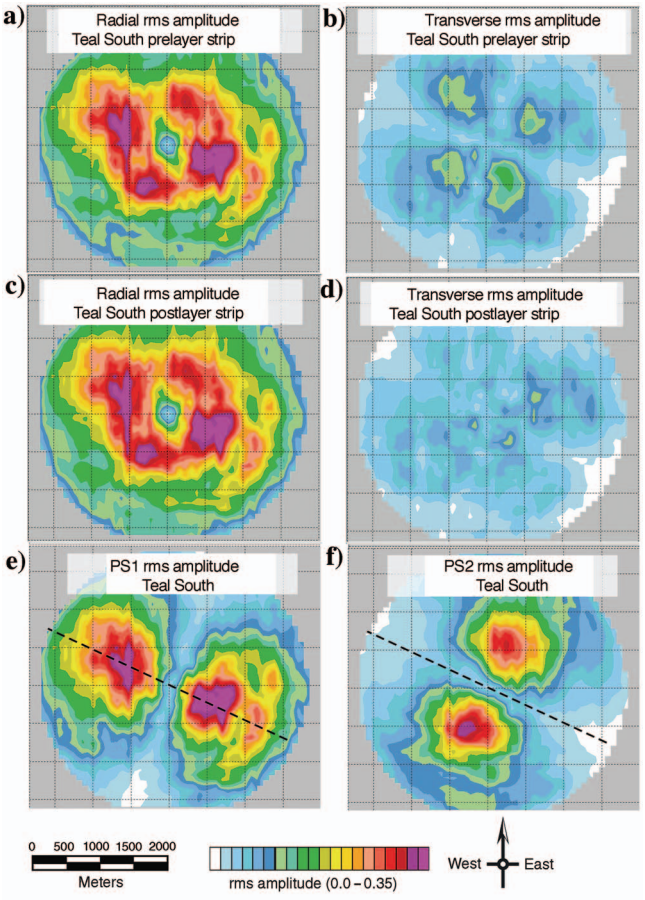

Figure 11. The rms amplitudes for radial and transverse components for a deeper event from the Teal South data set (event four) at approximately 1550 ms, which is characterized as anisotropic. (a) The rms amplitude of the radial component has developed a quadrapole pattern — with amplitudes aligned at 115°, indicating anisotropy above the reflection. b) The rms amplitude of the transverse component is a quadrapole with nulls aligned with the strike. (c) Radial component after layer stripping. (d) Transverse component after layer stripping. rms amplitudes of the transverse component have been minimized. (e) PS1 rotated to 115° and (f) PS2.

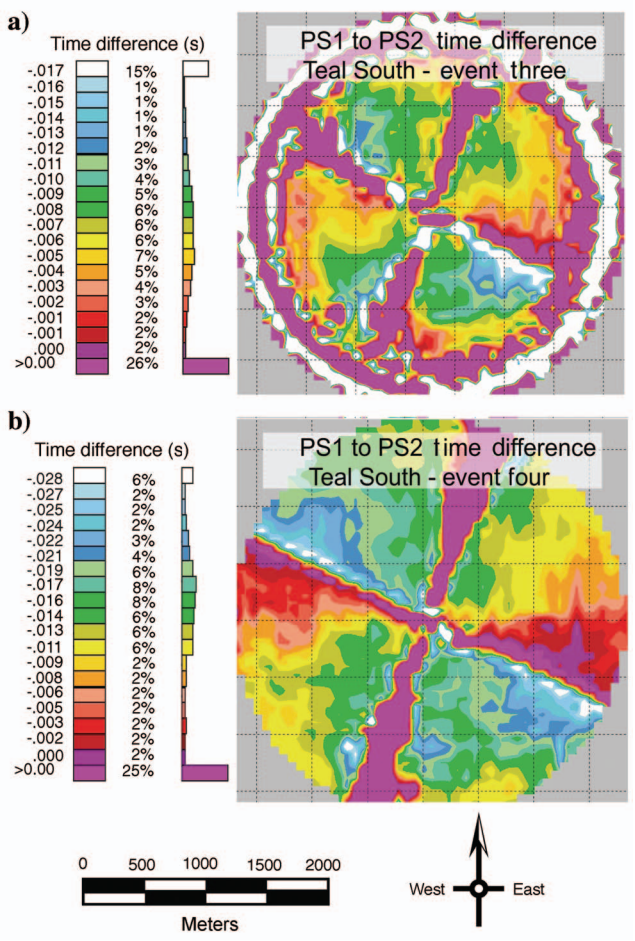

Figure 12. PS1 to PS2 time-difference map for events three and four. (a) Event three: Time differences range from −18 to 0 ms, except on principal axes. The average is ~7.5 ms. (b) Time differences range from −28 to 0 ms, with the average at ~17 ms.

DISCUSSION AND CONCLUSION

Constant time shifts are not adequate for prestack layer stripping because they induce distortions in amplitudes that adversely affect inversion. It is important to avoid principal directions when measuring traveltime differences, because this will produce null values; however, adequate azimuthal coverage is needed for accurate inversion and also to determine the symmetry axes. We show that although zero-offset techniques are fairly robust when applied to poststack data, they ignore the wealth of azimuthal and offset traveltime information contained in prestack data that may be used to enhance both imaging and fracture characterization.

After prestack layer stripping of modeled HTI and TTI media, several observations were made. In HTI media:

1) Radial and transverse components exhibit incorrect symmetry and orientation, as well as distortions in amplitudes.
2) In the case of PS1 and PS2 components, although symmetry and orientation are correct, the amplitudes are incorrect.
3) Layer-stripped and isotropic time differences resulting from birefringence, are similar for near offsets and along fracture strike, but dissimilar at far offsets normal to fracture strike. This traveltime-difference anomaly has two planes of symmetry oriented with and symmetric about the fractures.

For TTI media:

1) Radial and transverse components exhibit incorrect symmetry and orientation, as well as distortions in amplitudes.
2) In the case of PS1 and PS2 components, incorrect symmetry, orientation, and amplitudes are incorrect.
3) Time-difference comparisons between a layer-stripped TTI model and an isotropic model are similar to HTI media; however, the time-difference anomaly is asymmetric with only one plane of symmetry normal to the fracture strike direction. The time difference between the anisotropic model with bulk time shift corrections applied and the isotropic model increases down dip and decreases up dip.

Analysis of the Teal South data has shown that the amplitude maps exhibit traits associated with either a HTI or shallow-dipping TTI system and that the layer-stripping method behaves similarly on the real data as in the models. Analysis agrees with a previous Alford rotation analysis in terms of strike direction, as well as an average, zero-offset birefringence determination using crosscorrelation.

We recommend developing a prestack approach that would capitalize on the azimuthal and offset variations inherent in the S-wave birefringence. Such a technique necessarily must avoid the principal axes of the media where no time difference data are observable but must extrapolate observable data to obtain a time-difference surface map.

Once achieved, the offset and azimuthal variations in time difference may be applied to the data, instead of a simple bulk shift. Because information from orthogonal azimuths is needed for 4-C rotation analysis in prestack PS-wave data, the process may be improved by starting initially with a 4-C rotation algorithm applied to near offsets only for determination of fracture strike or symmetry direction and then utilizing a more simplistic two component (2-C) rotation algorithm to rotate from a radial transverse coordinate system to a natural (PS1 and PS2, in this case) coordinate system, and back again as needed.

ACKNOWLEDGMENTS

This work was supported by the Petroleum Research Fund of the American Chemical Society (Contract Number 39906-AC8) and the members of the industry sponsored EDGER Forum. We are indebted to Robert Tatham for his invaluable guidance throughout this project. We also thank Richard Van Dok, Subhashis Mallick, and everyone involved at WesternGeco. We acknowledge WesternGeco for the use of their Omega™ software. Thanks also to Tom Davis and everyone at the RCP at the Colorado School of Mines for continued collaboration. We also acknowledge the associate editor and the anonymous reviewers for their important comments and suggestions.

REFERENCES

Alford, R. M., 1986, Shear data in the presence of azimuthal anisotropy: Dilley, Texas: 56th Annual International Meeting, SEG, Expanded Abstracts, 476–479.
Alkahlifah, T., and I. Tsvankin, 1995, Velocity analysis for transversely isotropic media: Geophysics **60**, 1550–1566.
Bakulin, A., V. Grechka, and I. Tsvankin, 2000, Estimation of fracture parameters from reflection seismic data — Part I: HTI model due to a single

fracture set: Geophysics, **65**, 1788–1802.
Cheret, T., R. Bale, and W. S. Leaney, 2000, Parameterization of polar anisotropic moveout for converted waves: 70th Annual International Meeting, SEG, Expanded Abstracts, 1181–1184.
Crampin, S., 1977, A review of the effects of anisotropic layering on the propagation of seismic waves: Geophysical Journal of the Royal Astronomical Society, **49**, 9–27.
———, 1978, Seismic-wave propagation through a cracked solid: Polarization as a possible dilatancy diagnostic: Geophysical Journal of the Royal Astronomical Society, **53**, 467–496.
———, 1981, A review of wave motion in anisotropic and cracked elastic-media: Wave Motion, **3**, 343–391.
———, 1985, Evidence for aligned cracks in the earth's crust: First Break 03, 12–15.
Gaiser, J. E., 1997, 3-D Converted shear wave rotation with layer stripping: US Patent 5,610,875.
———, 1999, Applications for vector coordinate systems of converted waves obtained by multicomponent 3-D data: 31st Annual Offshore Technology Conference, OTC10985.
Gaiser, J., E. Loinger, H. B. Lynn, and L. Vetri, 2001, PS-Wave birefringence analysis at the Emilio Field for fracture characterization: 63rd Annual Conference and Exibition, EAGE, Extended Abstracts, Session N-07.
Gaiser, J. E., and R. Van Dok, 2003, PS-wave azimuthal anisotropy — seismic properties for fractured reservoir management: 65th Annual Conference and Exibition, EAGE, Extended Abstracts, Session N-07, EAGE, C22.
Helbig, K., 1958, Elastische Wellen in anisotropen Medien: Gerlands Beiträge zur Geophysik, **67**, 177–211; 256–288.
Hudson, J. A., 1981, Wave speeds and attenuation of elastic waves in materials containing cracks: Geophysical Journal of the Royal Astronomical Society, **64**, 133–150.
Lefeuvre, F., C. Cliet, and L. Nicoletis, 1989, Shear-wave birefringence measurement and detection in the Paris Basin: 59th Annual International Meeting, SEG, Expanded Abstracts, 786.
Lefeuvre, F., D. Winterstein, M. Meadows, and L. Nicoletis, 1991, Propagation matrix and layer-stripping methods: a comparison of shear-wave birefringence detection on two data sets from Railroad & apart Lost Hills fields: 61st Annual International Meeting, SEG, Expanded Abstracts, 55–60.
Lynn, H. B., 1991, Field measurements of azimuthal anisotropy: First 60 meters, San Francisco Bay area, CA, and estimation of the horizontal stresses' ratio from Vs1/Vs2: Geophysics, **56**, 822–832.
Lynn, H. B., 1992, Discussion on field measurements.
Lynn, H. B. and L. A. Thomsen, 1990, Reflection shear-wave data collected near the principal axes of azimuthal anisotropy: Geophysics, **55**, 147–156.
Mallick, S. and L. N. Frazer, 1987, Practical aspects of reflectivity modeling: Geophysics, **52**, 1355–1364.
Schoenberg, M., and J. Douma, 1988, Elastic wave propagation in media with parallel fractures and aligned cracks: Geophysical Prospecting, **36**, 571–590.
Stewart, R. R., J. E. Gaiser, J. R. Brown, and D. C. Lawton, 2003, Converted-wave seismic exploration: Applications: Geophysics, **68**, 40–57.
Tatham, R. H., and M. D. McCormack, 1991, Multicomponent seismology in petroleum exploration, multicomponent seismology in petroleum exploration: SEG, 248.
Thomsen, L., 1988, Reflection seismology over azimuthally anisotropic media: Geophysics, **53**, 304–313.
———, 1995, Elastic anisotropy due to aligned cracks on porous rock: Geophysical Prospecting, **43**, 805–829.
———, 2001, Vector recomposition of seismic 3-D converted-wave data: US Patent 6,292,754 B1.
Thomsen, L., I. Tsvankin, and M. C. Mueller, 1999, Coarse-layer stripping of vertically variable azimuthal anisotropy from shear-wave data: Geophysics, **64**, 1126–1138.
Winterstein, D. F., and M. A. Meadows, 1991a, Shear-wave polarizations and subsurface stress directions at Lost Hills field: Geophysics, **56**, 1331–1348.
———, 1991b, Changes in shear-wave polarization azimuth with depth in Cymric and Railroad Gap oil fields: Geophysics, **56**, 1349–1364.